Evidence of Mixed Scaling for Mean Profile Similarity in the Stable Atmospheric Surface Layer

MICHAEL HEISEL [a] AND MARCELO CHAMECKI [b]

[a] *School of Civil Engineering, University of Sydney, Sydney, New South Wales, Australia*
[b] *Department of Atmospheric and Oceanic Sciences, University of California, Los Angeles, Los Angeles, California*

ABSTRACT: A new mixed scaling parameter $Z = z/(Lh)^{1/2}$ is proposed for similarity in the stable atmospheric surface layer, where z is the height, L is the Obukhov length, and h is the boundary layer depth. In comparison with the parameter $\zeta = z/L$ from Monin–Obukhov similarity theory (MOST), the new parameter Z leads to improved mean profile similarity for wind speed and air temperature in large-eddy simulations. It also yields the same linear similarity relation for CASES-99 field measurements, including in the strongly stable (but still turbulent) regime where large deviations from MOST are observed. Results further suggest that similarity for turbulent energy dissipation rate depends on both Z and ζ. The proposed mixed scaling of Z and relevance of h can be explained by physical arguments related to the limit of z-less stratification that is reached asymptotically above the surface layer. The presented evidence and fitted similarity relations are promising, but the results and arguments are limited to a small sample of idealized stationary stable boundary layers. Corroboration is needed from independent datasets and analyses, including for complex and transient conditions not tested here.

KEYWORDS: Atmosphere; Boundary layer; Surface layer; Large-eddy simulations; Field experiments

1. Introduction

The wind speed and air temperature above Earth's surface are critical to both human activities and the interaction between Earth and the atmosphere. Accordingly, similarity in the shape of the mean profiles for these quantities is historically one of the most researched topics in the study of the atmospheric boundary layer (ABL). Under neutral conditions in the absence of a temperature gradient and other buoyancy effects, the wind speed is well described by the logarithmic law of the wall—or simply the "log law"—that can be derived using a variety of methods (see, e.g., von Kármán 1930; Prandtl 1932; Millikan 1938; Townsend 1976). A recent experimental assessment is provided by Marusic et al. (2013). In its gradient form, the log law is

$$\frac{\partial \overline{U}}{\partial z} = \frac{u_*}{\kappa z}, \tag{1}$$

where $\overline{U}$ is the mean horizontal wind speed, u_* is the friction (shear) velocity, κ is the von Kármán constant, and z is height above the surface. The log law is strictly valid in the lowest portion of the ABL known as the surface layer or inertial layer. While the surface layer is the focus of the present work, alternative incomplete similarity relations such as a wind speed power law are also common in various applications such as pollutant transport (Arya 1998), wind energy (Manwell et al. 2009), and wind engineering (Simiu and Yeo 2019) due to improved accuracy at higher positions above the surface layer (Barenblatt and Prostokishin 1993).

The prevailing framework to account for effects of temperature and buoyancy in the surface layer profiles comes from Monin–Obukhov similarity theory (MOST; Monin and Obukhov 1954). The theory postulates that the dimensionless gradients for wind speed (momentum)

$$\phi_m = \frac{\partial \overline{U}}{\partial z} \left(\frac{\kappa z}{u_*} \right) = f_m(\zeta) \tag{2}$$

and air temperature (heat)

$$\phi_h = \frac{\partial \overline{\theta}}{\partial z} \left(\frac{\kappa z}{\theta_*} \right) = f_h(\zeta) \tag{3}$$

are universal functions of the similarity parameter $\zeta = z/L$. The log-law scaling in Eq. (1) is used to normalize the gradients such that $\phi_m = 1$ in the absence of buoyancy. The Obukhov length (Obukhov 1971)

$$L = \frac{u_*^2 \overline{\theta}}{\kappa g \theta_*} \tag{4}$$

represents the height at which buoyancy mechanisms become important relative to shear based on scaling arguments for the turbulent kinetic energy (TKE) budget. Here, g is the gravitational constant. The functions $f_m(\zeta)$ and $f_h(\zeta)$ quantify deviations of the mean profiles from the log-law scaling and also connect the gradients to the surface fluxes for momentum $\overline{u'w'_s} = -u_*^2$ and heat $\overline{w'\theta'_s} = -u_* \theta_*$, respectively. MOST assumes that z and L are the only relevant length scales for the gradients in Eqs. (2) and (3), such that additional length scales including the surface roughness and ABL depth have negligible impact on the surface layer gradients.

For the stable atmospheric boundary layer (SBL) in weak stratification ($0 < \zeta \lesssim 1$), the consensus from early field

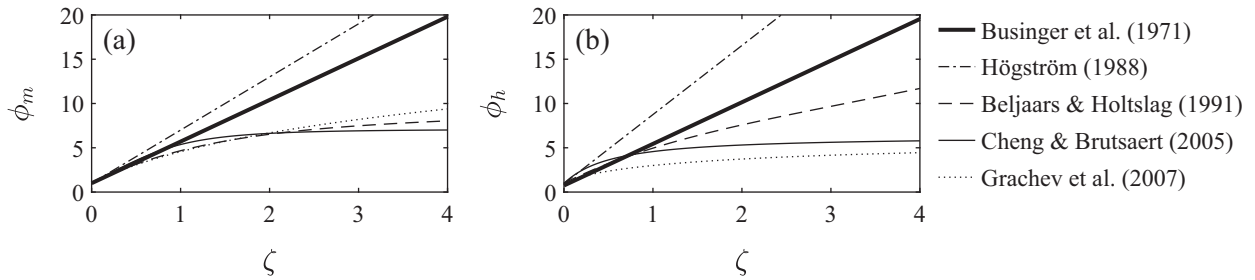*Corresponding author*: Michael Heisel, michael.heisel@sydney.edu.au

FIG. 1. Comparison of empirical similarity relations proposed in the literature for the stably stratified surface layer. The relations are used to predict the dimensionless mean gradient for (a) momentum $\phi_m = \partial \overline{U}/\partial z (\kappa z/u_*)$ and (b) heat $\phi_h = \partial \overline{\theta}/\partial z (\kappa z/\theta_*)$. Each relation is a function of the Monin–Obukhov similarity parameter $\zeta = z/L$, where L is the Obukhov length.

experiments is that $f_m(\zeta)$ and $f_h(\zeta)$ are linear functions (McVehil 1964; Zilitinkevich and Chalikov 1968; Webb 1970; Oke 1970; Businger et al. 1971; Dyer 1974) that result from a power series expansion in the original theory (Monin and Obukhov 1954). Upon integration of the gradient relations, the resulting mean profiles comprise a combination of logarithmic and linear components, where the linear contribution becomes dominant for large ζ in the limit of z-less stratification (Wyngaard and Coté 1972). However, numerous experiments have shown ϕ to deviate from the linear relations under increased stratification and become a weaker function of ζ for $\zeta > 1$ (Webb 1970; Beljaars and Holtslag 1991; Howell and Sun 1999; Grachev et al. 2005; Ha et al. 2007; Optis et al. 2014; among others). These observations have led to more complex functional forms for $f_m(\zeta)$ and $f_h(\zeta)$ that are approximately linear for weak stratification and capture the flattened trends for large ζ. A comparison of several empirical relations fitted to a variety of experimental datasets is shown in Fig. 1 (Businger et al. 1971; Högström 1988; Beljaars and Holtslag 1991; Cheng and Brutsaert 2005; Grachev et al. 2007).

Observed differences across the empirical relations in Fig. 1 are often attributed to experimental uncertainty (Yaglom 1977), the passage of large-scale eddies (Salesky and Anderson 2020), or the use of data periods in conditions where MOST is not valid (Kouznetsov and Zilitinkevich 2010). The latter point is particularly relevant for very stable conditions characterized by weak winds and global intermittency (Holtslag and Nieuwstadt 1986; Mahrt 1999). Previous works have shown that data points deviating from the linear trends are often associated with conditions exhibiting nonstationarity (Mahrt 2007) or a noncanonical energy spectrum without a clear inertial subrange (Grachev et al. 2013).

It is also possible that some of the variability in empirical fits is due to the relevance of additional parameter(s) such that ζ provides incomplete similarity. Zilitinkevich et al. used asymptotic matching arguments and generalized length scales to introduce dependencies on the Coriolis frequency f and properties of the capping inversion such as the Brunt–Väisälä frequency N (Zilitinkevich 1989; Zilitinkevich and Calanca 2000; Zilitinkevich and Esau 2005). The length scales associated with these frequencies, that is, u_*/f and u_*/N (Zilitinkevich and Esau 2005), are closely related to the equilibrium ABL depth h (Kitaigorodskii and Joffre 1988), which suggests ϕ may depend

on h in addition to L. Previous studies have introduced h into the similarity relations but have predominantly focused on augmenting MOST to capture trends above the surface layer (e.g., Gryning et al. 2007; Optis et al. 2014).

There is further research into the influence of h on stably stratified turbulence based on the transition between continuous and intermittent turbulence. Multiple parameters and knowledge of the overall boundary layer structure are required to predict the transition between these regimes (see, e.g., Williams et al. 2013; Monahan et al. 2015). In particular, simulations have shown that the critical point for the collapse of turbulence depends on both the stability and a bulk Reynolds number (Deusebio et al. 2015), and in certain cases h/L is explicitly used (van de Wiel et al. 2007; Donda et al. 2014). The role of h in the collapse of turbulence suggests it is a critical parameter to the phenomenology of stratified flows, and this idea is extended here to the fully turbulent regime through a reassessment of structural similarity.

In consideration of the variability seen in Fig. 1 and previous research into the importance of the boundary layer depth, the goal of the present study is to account for surface layer trends by expanding the parameter space of the similarity functions $\phi = f(z, L, h)$ to include h. Specifically, a revised similarity parameter $Z = z/\sqrt{Lh}$ [i.e., $Z = z/(Lh)^{1/2}$] is proposed based on a composite length scale using the geometric mean of L and h. It will be shown that Z provides improved similarity relative to traditional MOST for high-resolution large-eddy simulations (LES) (Sullivan et al. 2016) and yields a linear trend extending to strongly stable (but still turbulent) conditions in measurements from the 1999 Cooperative Atmosphere–Surface Exchange Study (CASES-99) field campaign (Poulos et al. 2002). A physical basis for the composite length scale $(Lh)^{1/2}$ is proposed that considers the profiles to asymptotically approach a z-less gradient above the surface layer and utilizes observed stability relations for resistance laws.

A brief overview of the LES and CASES-99 measurements is provided in section 2. A comparison of $\phi(\zeta)$ and $\phi(Z)$ is then presented in section 3. A justification for the mixed scaling and the connection between $\phi(\zeta)$ and $\phi(Z)$ are discussed in section 4. Concluding remarks are given in section 5. A detailed account of the CASES-99 data analysis is reserved for the appendix.

2. Stable atmospheric boundary layer data

The following descriptions of the LES and field measurements in the subsections below are limited to a summary of the most relevant details. The LES was previously presented elsewhere (Sullivan et al. 2016; Heisel et al. 2023), and the CASES-99 field campaign has been discussed in numerous studies (see, e.g., Poulos et al. 2002; Sun et al. 2002; Banta et al. 2002; Cheng and Brutsaert 2005; Ha et al. 2007; among many others). A full account of details required to reproduce the analysis of CASES-99 measurements is given in the appendix.

a. Large-eddy simulations

The LES domain design and imposed boundary conditions are based on the GEWEX Atmospheric Boundary Layer Study (GABLS) benchmark case (see, e.g., Beare et al. 2006). Four stability cases were achieved by applying a fixed surface cooling rate that ranged from $C_r = 0.25$ to 1 K h^{-1} across the different cases. The results presented here are based on average flow statistics between 8 and 9 physical hours of simulation when the ABL has reached near-equilibrium conditions except for a constant temperature shift owing to the fixed surface cooling (Sullivan et al. 2016). The conditions represent a simplified canonical case of a long-lived stable ABL. The 1024^3 numerical grid for each case corresponds to an isotropic resolution of $\Delta = 0.39$ m, noting the effective horizontal resolution is coarser due to the dealiasing scheme (Sullivan et al. 2016). The stable ABL cases are supplemented by a conventionally neutral simulation on a 512^3 grid (Heisel et al. 2023). The neutral case imposed zero surface heat flux and a stable capping inversion, such that weak buoyancy effects are present in the surface layer due to entrainment and downward propagation from the inversion. The conventionally neutral case is only included for later results that use local-in-height scaling.

The flux statistics for momentum $\overline{u'w'}$ and kinematic temperature $\overline{w'\theta'}$ are based on the sum of the resolved and subgrid-scale components. Further, the velocity statistics $\overline{U}$ and $\overline{u'w'}$ are calculated as the magnitude of the horizontal components along x and y to account for the moderate wind veer that is present in the surface layer. The ABL depth $h = z(-\overline{u'w'} = 0.05u_*^2)/0.95$ is estimated based on the height where the average shear stress is 5% of the surface value (Kosović and Curry 2000). The relevant scaling parameters for the conventionally neutral and stably stratified ABL are given in Table 1. In later figures, the cases are classified based on the stability parameter h/L.

Gradients of the mean profiles are computed using centered finite difference evaluated at the midheights between vertical grid points. Later results exclude statistics from the lowest 3% of the ABL relative to h, which is approximately the lowest 10 vertical grid points. Statistics within the excluded region exhibit "overshoot" and a clear dependence on the wall model (Mason and Thomson 1992; Brasseur and Wei 2010). The number of excluded grid points will depend on the employed subgrid-scale and wall models, such that the

TABLE 1. Key scaling parameters from large-eddy simulations of the ABL under conventionally neutral (Heisel et al. 2023) and stably stratified (Sullivan et al. 2016) conditions. Here, h is the ABL depth based on the flux profile decay, L is the Obukhov length, u_* is the friction velocity, θ_* is the surface temperature scaling, and Δ_z is the LES grid resolution along the vertical direction.

h/L	h (m)	L (m)	u_* (m s^{-1})	θ_* (K)	Δ_z/h
0.0	258	$O(10^5)$	0.33	0.000	0.0030
1.4	160	116	0.26	0.038	0.0024
1.8	136	75	0.23	0.049	0.0029
2.2	122	55	0.22	0.061	0.0032
3.5	89	26	0.19	0.100	0.0044

appropriate cutoff should be evaluated independently in future studies.

b. CASES-99 field measurements

The CASES-99 field campaign occurred during October 1999 over flat grassland in southeastern Kansas (Poulos et al. 2002). Numerous measurement systems were deployed, including a 60-m-tall meteorological (hereinafter "met") tower. The tower was instrumented with 8 sonic anemometers ranging from 1.5 to 55 m above ground level, 6 vane anemometers, 6 thermistors, and 34 thermocouples.

Mean and turbulent statistics are calculated from 5-min data periods that meet quality control criteria. Turbulent flux statistics are computed exclusively using the sonic anemometers because of the high sampling rate of 20 Hz and their simultaneous measurement of velocity and temperature. The scaling parameters u_*, θ_*, and h are estimated by fitting idealized nondimensional flux profiles (Nieuwstadt 1984) to the measurements. The fitting procedure limits the analysis to conditions with a decaying flux across the height of the met tower, thus excluding periods exhibiting pronounced "top-down" turbulence and other more complex vertical structure (Mahrt and Acevedo 2023). The appendix material outlines in further detail the quality control criteria, flux profile fitting procedure, and methods employed to estimate flux-gradient statistics.

3. Results

a. Surface scaling

The nondimensional gradients for momentum in Eq. (2) and heat in Eq. (3) are shown as a function of ζ in Figs. 2a and 2b, respectively, for the LES cases in Table 1. The conventionally neutral case is excluded here for the evaluation of surface scaling, but is included in later results. Surface scaling refers to the traditional definition of ϕ and L using surface fluxes u_* and θ_*. The value $\kappa = 0.4$ is used for the von Kármán constant. Heights between $z = 0.03h$ and $0.3h$ are included in Fig. 2 and later plots. The maximum height is above the traditional limit of the surface layer (i.e., $0.1h$, indicated for reference in each figure). The range is extended to $0.3h$ because the observed surface layer trends continue to this height, including a local equilibrium in the TKE budget seen in later results.
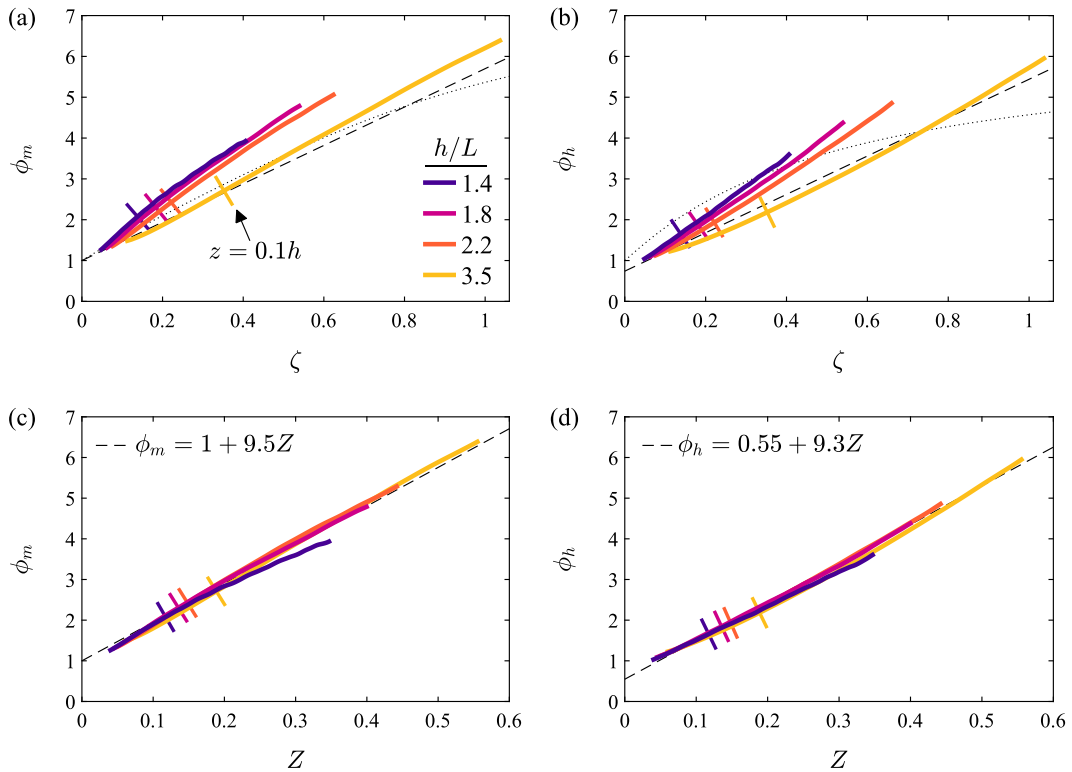
FIG. 2. Comparison of the traditional similarity parameter $\zeta = z/L$ and the proposed parameter $Z = z/(Lh)^{1/2}$ for the simulations of the stable ABL in Table 1: (a) $\phi_m(\zeta)$, (b) $\phi_h(\zeta)$, (c) $\phi_m(Z)$, and (d) $\phi_h(Z)$. Vertical positions from $z = 0.03h$ to $0.3h$ are included here, and the short lines indicate the height $z = 0.1h$ for reference. The reference lines in (a) and (b) are the $\phi(\zeta)$ expressions from Businger et al. (1971; dashed) in Eq. (5) and Cheng and Brutsaert (2005; dotted) in Eq. (6). The relations in (c) and (d) result from a least squares fit to the LES. Different colors in this and later figures correspond to variability in h/L.

Two empirical similarity relations from Fig. 1 are included in Figs. 2a and 2b for reference. The relations from Businger et al. (1971, dashed lines) are

$$\phi_m(\zeta) = 1 + 4.7\zeta \qquad \text{and}$$

$$\phi_h(\zeta) = 0.74 + 4.7\zeta. \tag{5}$$

The function from Cheng and Brutsaert (2005, dotted lines) is

$$\phi(\zeta) = 1 + a\left[\frac{\zeta + \zeta^b(1 + \zeta^b)^{(1-b)/b}}{\zeta + (1 + \zeta^b)^{1/b}}\right], \tag{6}$$

where $a = 6.1$ and $b = 2.5$ for ϕ_m and $a = 5.3$ and $b = 1.1$ for ϕ_h. The expression is designed to account for observed trends in the strongly stable regime ($\zeta > 1$) and is used in atmospheric models such as the Weather Research and Forecasting Model (Jiménez et al. 2012).

The MOST relations capture a majority of the deviation in the profiles from the neutral log-law scaling. See, for example, Fig. 1 of Heisel et al. (2023). However, the residual differences in Figs. 2a and 2b exhibit a clear stability trend. The order of the cases, i.e., decreasing ϕ with increasing bulk stability,

suggests that MOST overcompensates for the effect of stable stratification on the gradients for the conditions simulated by the LES. Previous works have identified similar stability trends and noted the possibility for an h/L correction in convective conditions (Khanna and Brasseur 1997; Johansson et al. 2001; Salesky and Chamecki 2012).

The similarity can be improved by weakening the dependence on L in the revised parameter $Z = z/(Lh)^{1/2}$. Incorporating the SBL depth h in Z is another critical component for the collapse of profiles throughout the surface layer and up to $0.3h$ as seen in Figs. 2c and 2d. For instance, using h defined from the flux profiles leads to greater similarity relative to alternate representations of the SBL depth such as the inversion layer height z_i (not shown), which varies more weakly with stratification. The profiles exhibit weak curvature but are well approximated by the fitted linear relations

$$\phi_m(Z) = 1 + 9.5Z \qquad \text{and}$$

$$\phi_h(Z) = 0.55 + 9.3Z. \tag{7}$$

The intercept of 1 for $\phi_m(Z)$ is imposed to match the log law for neutral conditions and is 0.9 if the fit is unconstrained. The intercept for ϕ_h is 0.72 if only heights below $0.1h$ are considered, where the difference is due to the weak convex curvature

TABLE 2. The normalized mean square error (NSME) and correlation coefficient ρ quantifying the alignment of the observed ϕ values with those predicted by empirical similarity relations: surface scaling for ϕ_m and ϕ_h in Figs. 2 and 3, local scaling Φ_m and Φ_h in Fig. 4, and local scaling for dissipation Φ_ϵ in Fig. 5. The similarity relations are defined in Eq. (5) for Businger et al. (1971), in Eq. (6) for Cheng and Brutsaert (2005), and in the corresponding figures for the proposed parameter $Z = z/(Lh)^{1/2}$.

		NMSE			Correlation		
		Businger et al. (1971)	Cheng and Brutsaert (2005)	$f(Z)$ (present)	Businger et al. (1971)	Cheng and Brutsaert (2005)	$f(Z)$ (present)
LES	ϕ_m	0.059	0.035	0.001	0.96	0.97	>0.99
	ϕ_h	0.041	0.029	0.001	0.96	0.96	>0.99
	Φ_m	0.059	0.054	0.001	0.97	0.98	>0.99
	Φ_h	0.031	0.035	0.001	0.97	0.95	>0.99
	$\Phi_\epsilon = \Phi_m - \zeta$	0.072	0.066	0.003	0.95	0.96	>0.99
CASES-99	ϕ_m	0.46	0.23	0.13	0.89	0.87	0.93
	ϕ_h	0.73	0.35	0.25	0.77	0.81	0.84
	Φ_m	0.95	0.35	0.12	0.87	0.83	0.93
	Φ_h	1.98	0.38	0.29	0.73	0.77	0.81

across the extended range of heights. The interpretation of the fitted intercept and slope values is further discussed later. The more important outcome of Fig. 2 is the markedly improved collapse of profiles corresponding to $\phi(Z)$.

Table 2 quantifies the agreement between the observed ϕ values and those predicted by the empirical relations featured in Fig. 2. The normalized mean squared error (NMSE; Chang and Hanna 2004) measures the goodness of fit, and the correlation coefficient ρ is a metric for data scatter irrespective of systematic error. The low NMSE and $\rho > 0.99$ values for the revised similarity parameter are consistent with the close overlap of profiles seen in Figs. 2c and 2d.

Figure 3 shows the same statistics as Fig. 2, except the CASES-99 field measurements are featured rather than the LES. Figure 3 employs the same upper height limit of $z = 0.3h$ as before. A significantly wider range of ζ and Z values is observed relative to Fig. 2, thus extending the similarity scaling comparison from weak and moderate stratification to more stable conditions. The wider range is also apparent from the estimated bulk stability h/L indicated by the color of each data marker in Fig. 3, where the range of h/L values is due to large variability in both h and L across 5-min periods (see, e.g., Fig. A2). Traditional MOST and the proposed mixed scaling parameter are related as $Z = \zeta(h/L)^{-1/2}$, such that the difference between ζ and Z increases with increasing h/L. This trend is observed in Figs. 3a and 3b, where the deviation from a linear regression is predominately due to strongly stable periods with large h/L. Further, the flattening of the trend with increasing h/L yields a curve resembling the nonlinear functions in Fig. 1. The curvature results in high NMSE values in Table 2 for the linear Businger et al. (1971) relations.

The mixed scaling parameter Z in Figs. 3c and 3d compensates for the observed h/L dependence and produces a $\phi(Z)$ relation that is approximately linear within the scatter of the data markers. Based on the consistently lower NMSE and higher ρ values in Table 2, the expressions in Eq. (7) align well with the field measurements, despite being fitted to the LES data that are confined to lower ζ and Z values. The alignment of Eq. (7) with the LES and CASES-99 data across a wide range of stable stratification and the reduction in scatter

suggest that the composite length $(Lh)^{1/2}$ is a relevant scaling parameter for the mean profiles in both weakly and strongly stratified conditions, excluding the regime of intermittent turbulence that is not assessed here.

The similarity of $\phi(Z)$ for weak stratification is specific to the LES results in Figs. 2c and 2d. For the field data in Fig. 3, the scatter and uncertainty of the results exceed any differences between ζ and Z for weakly stable conditions (e.g., $\zeta < 1$). Further, many of the points in this regime appear to fall below the reference curves. The analysis outlined in the appendix is not optimized for identifying and assessing periods of weak stratification, particularly when h is well above the tower height. Longer data periods, stricter stationarity criteria, and an alternative procedure for estimating h would all help to refine the statistics for weak stratification. In this context, conclusions drawn from Fig. 3 are limited to the pronounced and well-defined trends for large h/L.

One caveat to the trends in Fig. 3 is self-correlation due to shared terms in the nondimensional parameters (Kenney 1982); e.g., u_* appears in both ϕ_m and ζ. To test this effect, the values for the dimensional gradients $\partial \overline{U}/\partial z$ and $\partial \overline{\theta}/\partial z$ were randomized across the observations (Hicks 1981; Klipp and Mahrt 2004), while fixing the scaling parameters to preserve their correlations. The randomized momentum results yielded similar levels of self-correlation: $\rho \approx 0.7$ for ζ and 0.75 for Z. However, the randomized heat values were weakly correlated for all cases, i.e., $\rho < 0.15$. While self-correlation likely contributes to part of the reduced scatter for momentum, it explains neither the high correlations for ϕ_h nor the alignment of Eq. (7) with both LES and CASES-99 data.

b. Local scaling

Many of the data points in Fig. 3, particularly for large h/L, correspond to the stability regime and range of heights where local-in-height scaling is recommended (Nieuwstadt 1984; Sorbjan 1986). Accordingly, the results in Figs. 2 and 3 are reevaluated in Fig. 4 using local scaling parameters, including for the conventionally neutral LES case. Specifically, the nondimensional gradients Φ and local Obukhov length $\Lambda(z)$ are
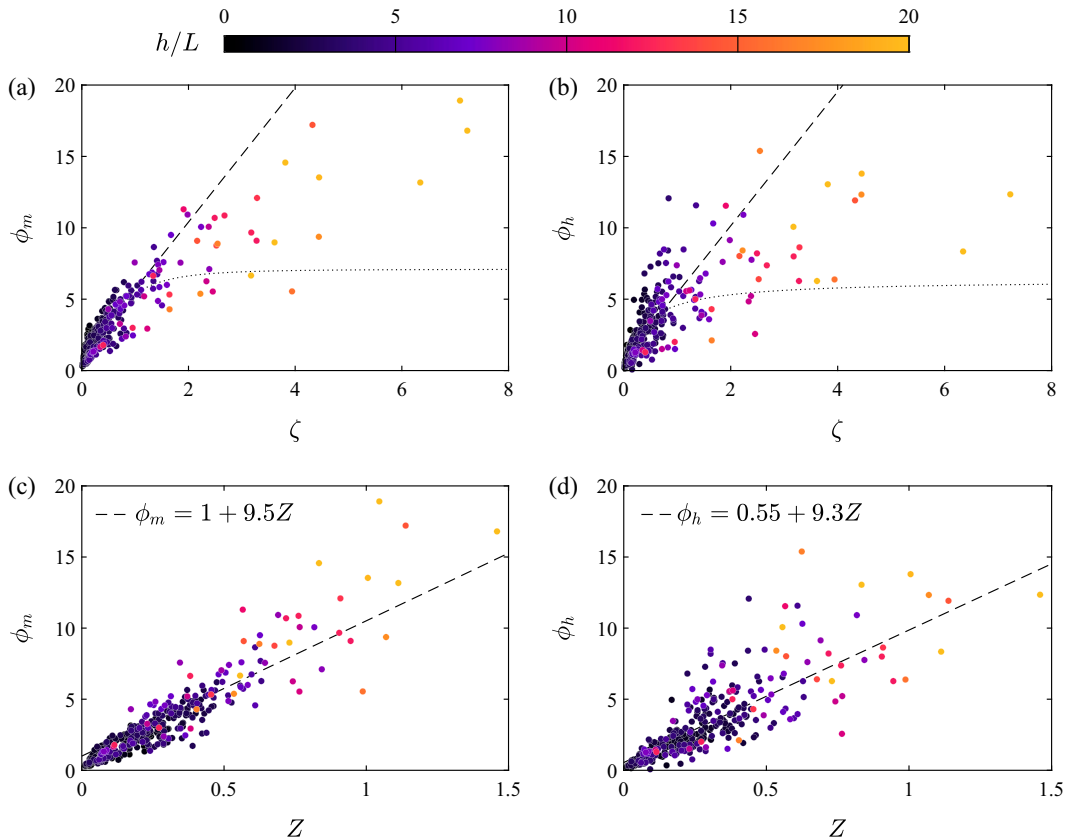
FIG. 3. Comparison of the traditional similarity parameter $\zeta = z/L$ and the proposed parameter $Z = z/(Lh)^{1/2}$ for CASES-99 field measurements in stable conditions: (a) $\phi_m(\zeta)$, (b) $\phi_h(\zeta)$, (c) $\phi_m(Z)$, and (d) $\phi_h(Z)$. Vertical positions up to $z = 0.3h$ are included here, and symbol color indicates the estimated h/L value. The reference lines in (a) and (b) are the $\phi(\zeta)$ expressions from Businger et al. (1971; dashed) in Eq. (5) and Cheng and Brutsaert (2005; dotted) in Eq. (6). The relations in (c) and (d) correspond to linear fits to the LES shown in Figs. 2c and 2d and Eq. (7).

now defined using $\overline{u'w'}(z)$ and $\overline{w'\theta'}(z)$ in place of u_* and θ_*. For the CASES-99 results in the inset panels, the local fluxes correspond to those computed directly from the sonic anemometers and not the value of the fitted flux profile at the same height.

As seen in Figs. 4a and 4b, local scaling does not account for the h/L trends observed for $\phi(\zeta)$ in previous figures. There remains a marked discrepancy for the most stable LES case with $h/L = 3.5$, and local scaling underestimates the buoyancy effects for the conventionally neutral case with $h/L \ll 1$. For the CASES-99 results, there is no discernible difference between $\Phi(z/\Lambda)$ and the previous results in Figs. 3a and 3b. In both Figs. 3 and 4, the proposed similarity parameter has lower NMSE values regardless of whether surface or local scaling is employed. The improved similarity with Z in previous figures therefore cannot be explained by Z better representing the local nondimensional parameters and their height-dependent properties.

As before, the mixed scaling parameter $z/\sqrt{\Lambda h}$ yields a complete collapse of the LES profiles in Figs. 4c and 4d, suggesting mean profile similarity is better represented by $\Phi(z/\sqrt{\Lambda h})$ than $\Phi(z/\Lambda)$. The local scaling also appears to

account for the weak curvature seen in Fig. 2 and produces an unambiguously linear dependence. The collapse in Figs. 4c and 4d includes the traditional surface layer below $z = 0.1h$ and the conventionally neutral case with top-down stability effects. In the geometric mean $(Lh)^{1/2}$, the depth h has a strong modulating effect on extreme values of L: h significantly decreases Z for $h/L \gg 1$ in strongly stable conditions (Fig. 3) and increases Z for $h/L \ll 1$ in near-neutral conditions (Fig. 4). This modulation brings the results into alignment with the linear trend across the full range of $z/\sqrt{\Lambda h}$ tested here. In contrast, alternate combined length formulations such as an inverse summation length scale (e.g., Delage 1974; Zilitinkevich and Esau 2005) always favor the small values and are less successful in capturing the trends observed here.

c. Dissipation

To interpret the origin of the composite length scale $(Lh)^{1/2}$, it is informative to consider the dissipation rate ϵ of TKE. For conditions in a local equilibrium between shear production $P = -\overline{u'w'}\,\partial \overline{U}/\partial z$, buoyancy production (destruction) $B = g\overline{w'\theta'}/\overline{\theta}$, and dissipation ϵ, the nondimensional
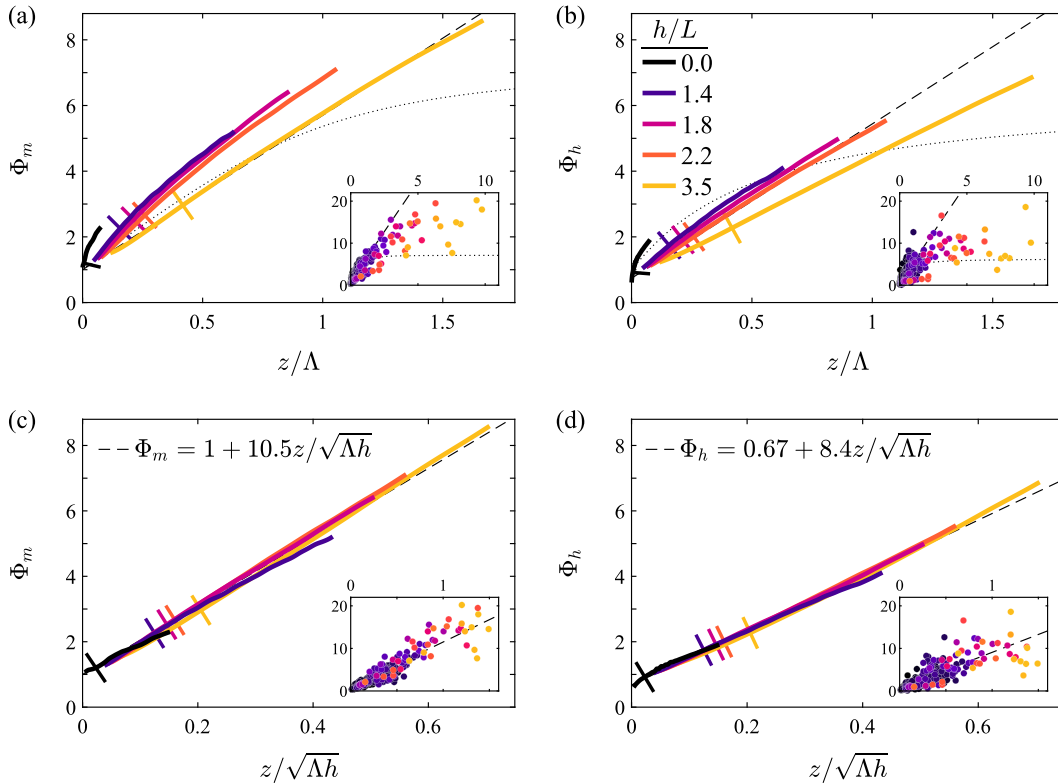
FIG. 4. As in Figs. 2 and 3, except the dimensionless gradients Φ and Obukhov length Λ are defined using local-in-height fluxes rather than surface parameters, including for the conventionally neutral LES case. Vertical positions from $z = 0.03h$ to $0.3h$ are included here, and the short lines indicate the height $z = 0.1h$ for reference. The reference lines in (a) and (b) are the $\phi(\zeta)$ expressions from Businger et al. (1971; dashed) in Eq. (5) and Cheng and Brutsaert (2005; dotted) in Eq. (6). The relations in (c) and (d) result from a least squares fit to the LES.

TKE budget reduces to (e.g., Hartogensis and de Bruin 2005)

$$0 = \Phi_m - \frac{z}{\Lambda} - \Phi_\epsilon, \qquad (8)$$

where Φ_m arises from production P, z/Λ represents B, and $\Phi_\epsilon = \epsilon \kappa z / (-\overline{u'w'})^{3/2}$. Equation (8) can also be expressed in terms of surface scaling if the local fluxes in P and B are assumed to be equivalent to the surface parameters. Local fluxes are used here due to the observed flux decay throughout the surface layer. If $z/\sqrt{\Lambda h}$ is the appropriate similarity parameter for Φ_m as evidenced in Fig. 4, then Eq. (8) requires that Φ_ϵ be a function of both $z/\sqrt{\Lambda h}$ and z/Λ.

The dissipation dependence is evaluated in Fig. 5 for the LES data. Dissipation was also estimated for the CASES-99 measurements using the amplitude of the energy spectrum in the inertial subrange (Saddoughi and Veeravalli 1994). While the local equilibrium is often approximately observed in the stable surface layer (Wyngaard and Coté 1971; Chamecki et al. 2018) due to increasingly large values of shear production and dissipation (Wyngaard 1992; Frenzen and Vogel 2001), for many of the weakly stratified data periods an imbalance was observed between P, B, and ϵ such that Φ_ϵ did not adhere to

the expected trends. The imbalance may be due to a combination of nonstationarity in the TKE, contributions from transport terms that are neglected in Eq. (8), and uncertainties in Φ_ϵ estimates. Rather than selectively filtering the CASES-99 results to a smaller subset of the data that exhibits TKE equilibrium, the field measurements are excluded from Fig. 5.

The LES dissipation in Fig. 5 is modeled as $\epsilon = C_\epsilon e^{3/2}/\Delta$, where e is the subgrid-scale TKE and $C_\epsilon = 0.93$ (Moeng and Wyngaard 1988; Sullivan et al. 2016). The inset panel in Fig. 5a demonstrates the computed TKE equilibrium in the surface layer for each of the cases to support use of the simplified budget in Eq. (8). The dissipation in Figs. 5b and 5d is offset by z/Λ such that the resulting curves should match Φ_m from Figs. 4a and 4c. The $h/L = 3.5$ case in Fig. 5c is visibly displaced from the remaining curves, and the offset in Fig. 5d accounts for a majority of the observed displacement. Further, the result in Fig. 5d matches closely with Eq. (8) using the definition for $\Phi_m(z/\sqrt{\Lambda h})$ from the fitted relation in Fig. 4c.

The observed similarity in Fig. 5d implies that the composite length scale $\sqrt{\Lambda h}$ is specifically associated with the mean gradients $\partial \overline{U}/\partial z$ and $\partial \overline{\theta}/\partial z$. The scaling is also reflected by integral-scale turbulent features related to the mean gradients (Heisel et al. 2023), as will be discussed in section 4. The turbulent energy is predominantly set by these integral-scale features and
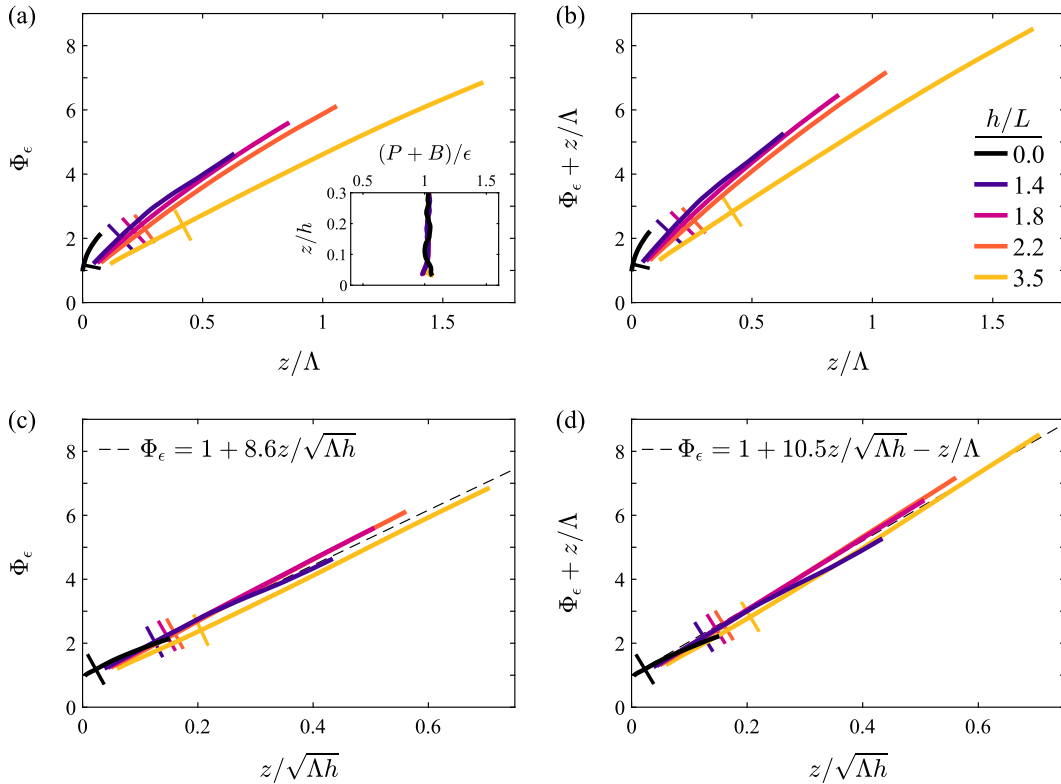
FIG. 5. Comparison of the dimensionless dissipation $\Phi_\epsilon = \epsilon \kappa z / (-\overline{u'w'})^{3/2}$ for the LES cases as a function of the traditional similarity parameter z/Λ and the proposed parameter $z/\sqrt{\Lambda h}$, where Φ and Λ are defined using local-in-height fluxes: (a) $\Phi_\epsilon(z/\Lambda)$, (b) $\Phi_\epsilon(z/\Lambda) + z/\Lambda$, (c) $\Phi_\epsilon(z/\sqrt{\Lambda h})$, and (d) $\Phi_\epsilon(z/\sqrt{\Lambda h}) + z/\Lambda$. Vertical positions from $z = 0.03h$ to $0.3h$ are included here, and the short lines indicate the height $z = 0.1h$ for reference. The results in (b) and (d) are offset by z/Λ according to the TKE equilibrium condition in Eq. (8). The inset panel of (a) shows the balance between TKE shear production P, buoyancy destruction B, and dissipation ϵ. The relations in (c) and (d) result from a least squares fit to the LES.

thus reflects the same mixed scaling as Φ_m. However, a fraction of the integral-scale energy proportional to z/Λ is directly dampened by negative buoyancy in stratified conditions. The remaining balance of the energy sets the required rate of small-scale dissipation in accordance with Eq. (8), where the balance depends strongly on $\sqrt{\Lambda h}$ through the shear production and has a weaker dependence on Λ owing to direct buoyancy effects. In other words, the rate of small-scale dissipation reflects a mixture of nondimensional similarity parameters resulting from competing large-scale effects.

4. Discussion

a. The limit of z-less stratification

The results in section 3 indicate the relevance of h to mean profile similarity in the surface layer, but the evidence thus far does not indicate *why* this should be the case. In fact, the idea that the surface layer is far from the influence of the upper boundary (i.e., $z \ll h$) is a common argument for excluding h as a relevant length scale in derivations of the log law. It is speculated here that this dependence originates from the limit of the mean gradients in z-less stratification.

Assuming a linear similarity relation for the SBL, the velocity gradient can be expressed as

$$\frac{\partial \overline{U}}{\partial z} \approx \frac{u_*}{\kappa z} + \left(\frac{\partial \overline{U}}{\partial z}\right)_{z-\text{less}}. \quad (9)$$

Log-law scaling is approximately achieved near the surface for small z when $u_*/(\kappa z)$ is the dominant term. Far from the surface and under strongly stratified conditions, the log-law gradient becomes relatively small and the result asymptotically approaches the z-less gradient with increasing height. This scaling behavior is also manifested by coherent features in the instantaneous turbulence. The size of the coherent regions is proportional to z in near-neutral conditions (Heisel et al. 2018, 2020) and decreases toward a constant value as stratification increases (Heisel et al. 2023). Equation (9) is further supported by the LES profiles featured in Fig. 6. Both the mean profiles in Figs. 6a and 6d and their gradients in Figs. 6b and 6e exhibit a strong dependence on z in the surface layer, and the gradients are approximately z-less throughout a large portion of the outer layer.

For MOST, the z-less gradient in Eq. (9) is proportional to u_*/L. While L quantifies the height at which buoyancy effects
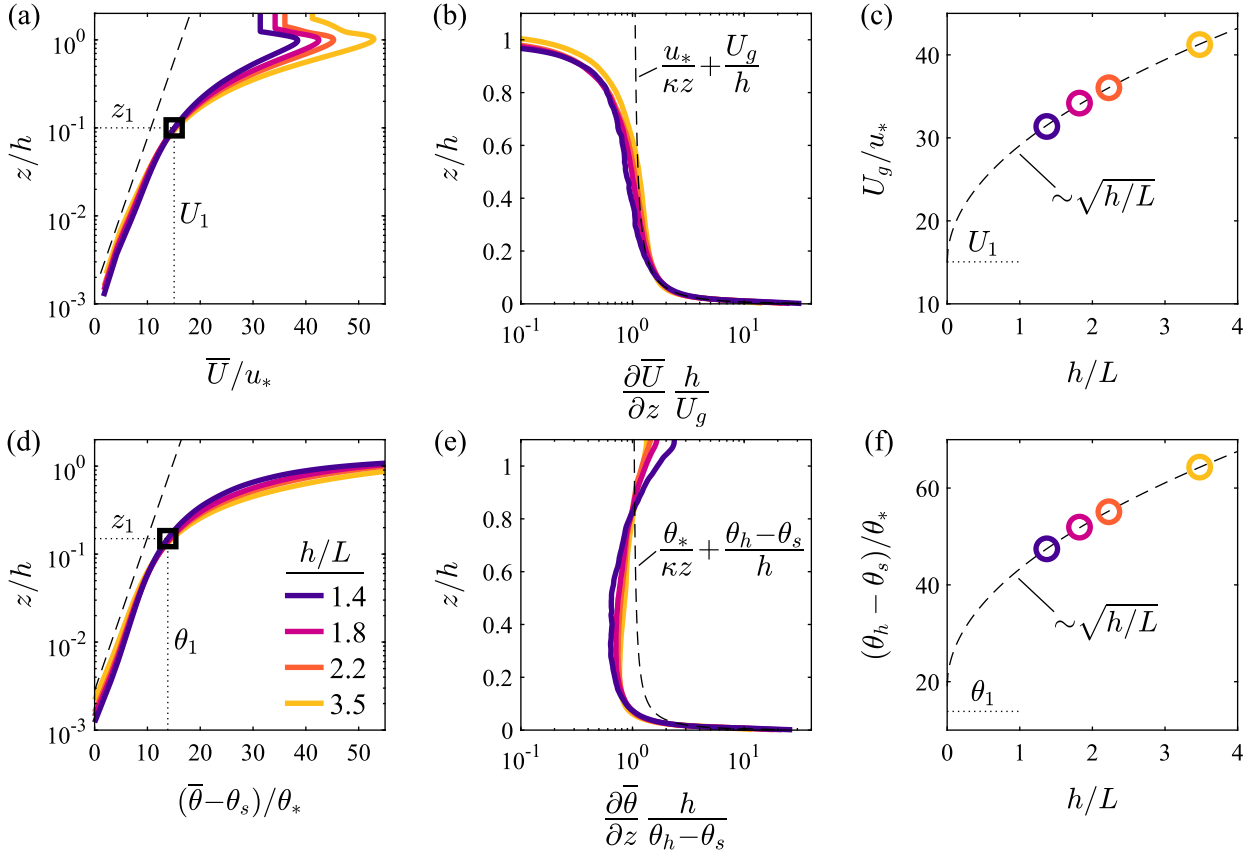
FIG. 6. Estimation of the bulk z-less gradient above the near-surface region: (left) approximate position where the mean profiles strongly deviate from log-linear scaling, (center) mean gradients relative to the bulk z-less approximation, and (right) bulk difference in velocity and temperature as a function of stability h/L for (a)–(c) velocity and (d)–(f) temperature, where U_g is the geostrophic wind speed, θ_h is the temperature at $z = h$, θ_s is the surface temperature, and subscript "1" indicates the properties at the estimated deviation points in the profiles. The dashed lines represent $\log(z)$ in (a) and (d), Eqs. (11) and (12) in (b) and (e), and $(h/L)^{1/2}$ in (c) and (f).

are important, it does not necessitate that the turbulence and statistics be directly proportional to L at any height. In this context, alternative scales such as the Ozmidov length have been proposed for stable conditions (Li et al. 2016). A simpler prediction is that the z-less gradient is constant throughout the depth of the SBL, leading to the value

$$\left(\frac{\partial \overline{U}}{\partial z}\right)_{z-\text{less}} \approx \frac{U_g}{h}, \tag{10}$$

where U_g is the geostrophic wind speed that describes the bulk velocity difference across h. While the speed of the low-level jet (LLJ) at height h is expected to be more representative than U_g in Eq. (10), the geostrophic wind speed is used here in order to relate the results to existing resistance laws. Substituting the Eq. (10) approximation into Eq. (9) yields

$$\frac{\partial \overline{U}}{\partial z} \approx \frac{u_*}{\kappa z}\left(1 + \kappa \frac{U_g}{u_*}\frac{z}{h}\right), \tag{11}$$

where u_*/U_g is the geostrophic drag coefficient predicted from resistance laws (Rossby and Montgomery 1935; LeHau 1959).

The same z-less approximation can be made for the temperature, resulting in

$$\frac{\partial \overline{\theta}}{\partial z} \approx \frac{\theta_*}{\kappa z}\left(1 + \kappa \frac{\theta_h - \theta_s}{\theta_*}\frac{z}{h}\right) \tag{12}$$

based on the temperatures θ_h at $z = h$ and θ_s at the surface.

Equations (11) and (12) are represented by dashed lines in Figs. 6b and 6e. The equations align well with the general shape of the profiles. The coarse z-less approximation employed here overpredicts the temperature gradient by 20%–30% in Fig. 6e, but this difference can be accounted for using a constant correction factor. Based on Figs. 6b and 6e, the relevance of h in the similarity relations results from an approximately z-less gradient directly above the surface layer that creates an asymptotic boundary condition expressed through Eq. (9).

The connection between the approximations in Eqs. (11) and (12) and the composite length scale $(Lh)^{1/2}$ relies on the resistance laws for drag U_g/u_* and heat transfer $(\theta_h - \theta_s)/\theta_*$. The stability dependence of these laws is evaluated in Figs. 6c and 6f. The trends closely match $(h/L)^{1/2}$ for both velocity and

temperature, such that the z-less terms in Eqs. (11) and (12) can be approximated as

$$\kappa \frac{U_g}{u_*} \frac{z}{h} \approx \kappa C_u \frac{z}{\sqrt{Lh}} \qquad \text{and}$$

$$\kappa \frac{\theta_h - \theta_s}{\theta_*} \frac{z}{h} \approx \kappa C_\theta \frac{z}{\sqrt{Lh}}. \qquad (13)$$

The dependence of the approximate z-less gradient on stratification therefore results in the same revised similarity parameter as Eq. (7). Based on the fitted coefficients $C_u = 14$ and $C_\theta = 24$ in the Figs. 6c and 6f curves, the constant factors in Eq. (13) are 5.6 and 9.7 for velocity and temperature, respectively. These values are reasonably similar to the slope factors in Eq. (7) in consideration of the coarse assumptions made here.

One notable assumption for the bulk z-less gradient is to neglect the effect of z scaling in the surface layer where the gradients are significantly greater than the z-less approximation. Excluding the surface layer from the z-less gradient leads to the revised approximations $(U_g - U_1)/(h - z_1)$ and $(\theta_h - \theta_1)/(h - z_1)$, where U_1 and θ_1 correspond to the estimated departure points from z scaling shown in Figs. 6a and 6d. These surface layer offsets U_1 and θ_1 account for a majority of the fitted intercepts in Figs. 6c and 6f, respectively, and help to explain the overprediction and small discrepancies seen in the outer layer in Figs. 6b and 6e.

Numerous previous works have studied the effect of stable stratification on U_g/u_* and $(\theta_h - \theta_s)/\theta_*$, where the stability parameter is typically $\mu = u_*/fL$ or $\mu = h/L$ (Melgarejo and Deardorff 1974). Many of the derived dependencies include a combination of $\log\mu$ and either μ or $\mu^{1/2}$ (e.g., Yamada 1976; Arya 1977; Du Vachat and Musson-Genon 1982; Byun 1991; Zilitinkevich and Esau 2005). The existence of resistance law functions with $\mu^{1/2}$ provides a precedent for the present observations. While the current results suggest that $(h/L)^{1/2}$ provides a good approximation for the resistance, the results are not conclusive due to the limited number of points in Figs. 6c and 6f and the complex parameter space of the resistance laws. In this context, the coefficients in Eqs. (7) and (13) may not be universal. Specifically, the fitted slopes may depend on additional factors such as f and N that are fixed across the present LES cases.

Another important consideration is that many derivations of the resistance laws invoke MOST in the surface layer as a boundary condition in order to determine the mean profiles aloft, such that a direct quantitative comparison cannot be made between the previous literature and the present discussion. This difference in approach is visualized in Fig. 7. Traditional derivations depicted in Fig. 7a use MOST relations in the surface layer and an upper boundary condition at $z = h$ to devise defect forms of the velocity and temperature profiles within the outer layer of the ABL (see, e.g., Byun 1991).

For the current approach shown in Fig. 7b, the presence of z-less stratification and an approximately constant gradient throughout a majority of the outer layer lead to a known matching condition in the vicinity of the surface layer. The
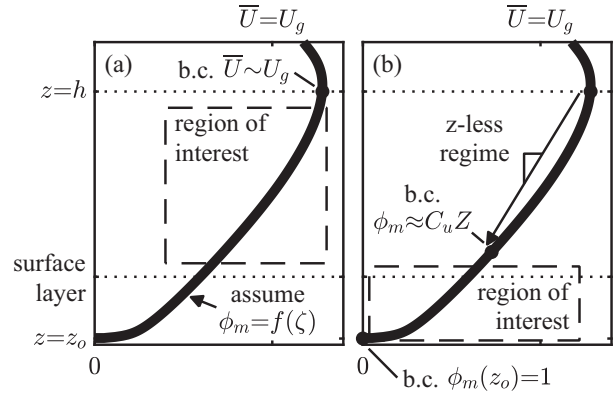

FIG. 7. Comparison of the (a) traditional and (b) proposed approach for matching similarity profiles in the ABL. In (a), profiles in the outer layer are designed to match MOST in the surface layer and satisfy the upper boundary condition (label b.c.) at $z = h$ (e.g., Byun 1991). In (b), the gradient in Eq. (13) is observed in the vicinity of the surface region due to approximately z-less stratification in the outer layer, such that the effect of h (through Z) cannot be neglected in the surface layer. The profile shown is the LES case with $h/L = 3.5$.

boundary condition is no longer far from the surface layer, such that the profiles in the surface layer must consider the influence of $(Lh)^{1/2}$ associated with the z-less gradient. The gradient profile in Eq. (9) matches both the surface condition $\phi_m \approx 1$ and the z-less gradient in the respective asymptotic limits $Z \ll 1$ and $Z \gg 1$, where the linear form of the similarity relation is supported by the evidence shown here and in the literature.

The proposed explanation for mixed scaling outlined in Fig. 7b applies also to the conventionally neutral LES case. A large portion of the outer layer in this case exhibits an approximately z-less mean velocity gradient owing to the top-down buoyancy effects (see, e.g., Fig. 1 of Heisel et al. 2023), where the flux Richardson number exceeds 0.1 throughout the top half of the ABL. The conventionally neutral case is thus expected to have the same z-less matching condition as the stable LES, except local scaling is required to account for the effect of the top-down stratification as seen in Fig. 4.

b. The shape of $\phi(\zeta)$

We return now to Fig. 1 to consider the nonlinear shape of $\phi(\zeta)$ and variability between fitted relations in the context of the proposed mixed length similarity. Assuming Z and the linear fit in Eq. (7) are the correct choice for mean profile similarity in the SBL, the dependence of the proposed similarity relations on ζ is

$$\phi\left(\zeta, \frac{h}{L}\right) = A + B\zeta\left(\frac{h}{L}\right)^{-1/2} \qquad (14)$$

for both momentum and heat, where A and B are assumed to be constants. The result is a linear relation for a given stability h/L whose slope decreases with increasing stability as seen in Figs. 2a and 2b.
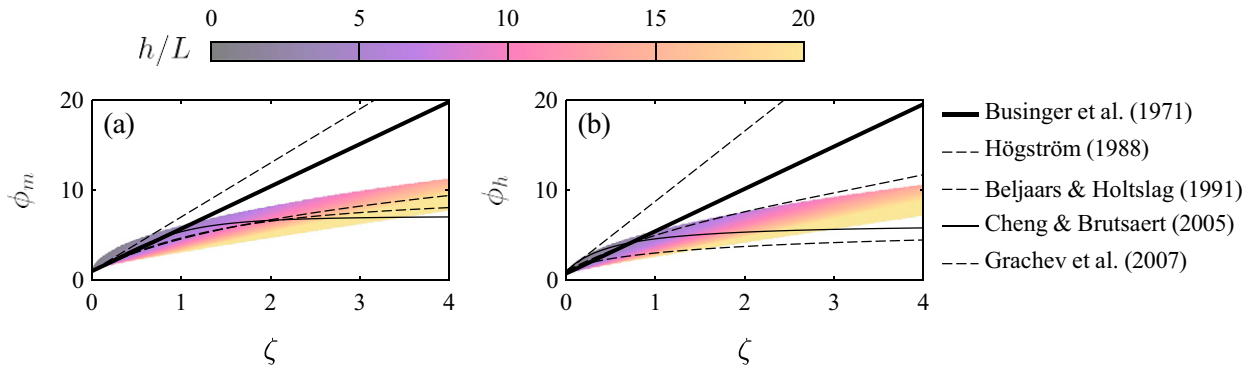
FIG. 8. As in Fig. 1, with the addition of $\phi(Z)$ curves projected onto the ζ–ϕ parameter space for a range of h/L conditions (colors) using the relations in Eq. (7). The resulting $\phi(\zeta)$ curves for a fixed h/L value are linear, but the linear trend is masked by the limited range of z/h that can be observed from typical field measurements (between $z = 1.5$ m and $0.3h$ in this example). The nonlinear shape of the colored band—resulting from the connection between Z, ζ, h, and L—closely resembles typical $\phi(\zeta)$ curves for strongly stable conditions.

In practice, the range of heights observed for a given stability h/L is selectively sampled based on measurement limitations. The lower bound of the range is given by either the lowest anemometer height or the depth of the roughness sublayer, and the upper bound is determined by either the tower height or the surface layer depth for shallow boundary layers. The effect of this range is visualized in Fig. 8, which shows Eq. (14) with h/L indicated by color and the solution confined to heights between $z = 1.5$ m and $0.3h$. Here, the SBL depth in meters is assumed to be $h = 1.25[40 − (h/L)]$ based on a weak linear trend observed from the CASES-99 results for large h/L, where the leading constant 1.25 has units of meters.

The selective height sampling discussed above acts as a bandpass filter on the solution space in Fig. 8, where the shape of the resulting band resembles the nonlinear empirical relations for $\phi(\zeta)$. This shape is determined by multiple factors. The most notable is the square root relation in Eq. (14), leading to $\phi \sim \zeta^{1/2}$ for a fixed z/h. The shape also depends on the relation between h and L for a given field site and the specific heights of the field instruments. The limits of the band move to lower values of ϕ if the measurement point is closer to the ground relative to h, which can correspond to either a lower anemometer position or a deeper SBL for a given L. In the same way, a higher measurement point or shallower SBL leads to higher observed ϕ values. The projection of the proposed similarity in Fig. 8 and its multiple dependencies may help to explain the observed nonlinearity in $\phi(\zeta)$ and some of the variability across different field campaigns.

5. Conclusions

The evidence presented here supports a composite length scale $(Lh)^{1/2}$ for similarity in the mean profiles of wind speed and air temperature under stable stratification. The mixed scaling combines the additional dependence on h into a single parameter Z that achieves improved similarity in mean gradients from LES of the SBL (Fig. 2). This similarity extends to LES of a conventionally neutral ABL when local-in-height scaling is considered (Fig. 4). For dissipation ϵ under equilibrium conditions, the similarity relations depend strongly on Z

and weakly on ζ (Fig. 5) in accordance with the TKE budget [Eq. (8)]. While traditional MOST and ζ can be used to predict a majority of the deviation from log-law scaling in the mean gradients and dissipation, the proposed similarity based on Z accounts for the remaining differences and matches closely with the profile trends as seen in Table 2.

The linear similarity relations in Eq. (7) fitted to the LES profiles align well with field measurements from the CASES-99 experiment, including for strong stability where a departure from MOST is often observed (Fig. 3). The shape of this departure in $\phi(\zeta)$ can be explained by the connection between Z and ζ [Eq. (14)] and the limited range of heights that can be sampled in experiments (Fig. 8).

It is speculated that the relevance of h to mean profile similarity in the surface layer may be related to approximately z-less stratification above the surface layer (Fig. 6), where the z-less limit may impose a boundary condition that influences the surface layer flow structure (Fig. 7). This dependence can be represented functionally by blending the log law with a z-less limit defined using upper boundary parameters [Eqs. (11) and (12)]. The proposed mixed scaling emerges from these functions after applying observed resistance relations [Eq. (13)].

The conceptual explanation of the mixed scaling and the similarity relations in Eq. (7) are considered to be preliminary efforts toward accounting for the trends observed here. Both the LES profiles and CASES-99 measurements support the linear relations

$$\phi_m(Z) = a_m + b_m Z,$$
$$\phi_h(Z) = a_h + b_h Z, \qquad \text{and}$$
$$\phi_\epsilon(Z, \zeta) = a_m + b_m Z - \zeta, \qquad (15)$$

where $a_m = 1$ is imposed to match the log-law scaling for neutral conditions and ϕ_ϵ is strictly valid under local equilibrium of TKE. Yet there is uncertainty in the value of the fitted parameters $b_{m,h}$ and a_h. The optimal values for the LES profiles are $b_m \approx 9.5$–10.5, $b_n \approx 8.4$–9.3, and $a_h \approx 0.55$–0.72, which all depend on the range of heights included in the fit and whether surface or local scaling is employed. If the arguments in

section 4 are valid, the slopes $b_{m,h}$ may exhibit some dependence on additional parameters relevant to the resistance laws such as f and N that were not tested here.

Further, the LES and field experiments both represent idealized stationary conditions and surface-forced turbulence. For instance, the CASES-99 data periods were selected based on idealized flux profiles that result from assumptions of stationarity and a constant Richardson number profile (Nieuwstadt 1984). These conditions are more common to long-lived boundary layers in polar and marine environments than traditional nocturnal boundary layers. The generality of the mixed scaling should therefore be corroborated and refined in future analyses, with specific scrutiny given to testing transient flow conditions, the appropriate intercept a_h, and the universality of $b_{m,h}$. However, it is expected that the evaluation of additional field measurements will be constrained by the requirement for a reliable estimation of the SBL depth.

Direct knowledge of h in the definition of Z can be avoided by using derived relations that consider the effects of rotation, stratification above the boundary layer, and surface-forced buoyancy (Zilitinkevich and Mironov 1996; Mironov and Fedorovich 2010). The limiting cases include $h \sim u_*/f$ for a neutral Ekman layer (Rossby and Montgomery 1935), $h \sim u_*/N$ for a conventionally neutral boundary layer with an overlying capping inversion (Kitaigorodskii and Joffre 1988), and $h \sim L$ for pure surface forcing in the absence of rotation (Kitaigorodskii 1960). While the last relation is derived invoking MOST in the surface layer, the same dependence occurs if L is replaced by $(hL)^{1/2}$, suggesting that the mixed scaling may reduce to traditional Monin–Obukhov similarity under specific simplified conditions. Importantly, each of these estimates represents the equilibrium depth. Under nonstationary conditions, the true depth—and the applicability of the mixed scaling as noted above—become more complicated (Nieuwstadt and Tennekes 1981).

Note also that the revised similarity can alternatively be expressed through multiple dimensionless parameters—for example, $\phi = f(\zeta, h/L)$ as seen in Eq. (14). The presence of multiple dependencies is consistent with the transition between stability regimes discussed in the introduction but does not comply with Buckingham π theorem (Buckingham 1914). Rather, it is a case of *similarity of the second kind* (Barenblatt 2003), where the exponent for each parameter cannot be determined directly by dimensional analysis. Here, the exponents in Eq. (14) were determined through empirical observation and are additionally supported by the physical arguments and results presented in section 4. These exponents are simplified into the single parameter Z to reduce the dimensionality of the similarity relations.

APPENDIX

Evaluation of CASES-99 Field Measurements

The CASES-99 database includes continuous met tower measurements spanning the duration of October 1999. The measurements were segmented into 5-min intervals to be individually evaluated and processed. Only nighttime data periods between 0000 and 1200 UTC (1900–0700 local time) were considered because of the higher likelihood of stably stratified conditions during these hours. The following additional criteria were evaluated for each 5-min period:

1) *The mean wind direction during the period was from 90° to 270°; that is, the wind was from east to west.* The tower anemometers faced to the east during CASES-99, and therefore winds toward the west are required for reliable measurements that are unobstructed by the meteorological tower. The relatively wide ±90° allowable wind range was chosen in consideration of the predominant wind directions of approximately 90° and 270° observed across all measurements.

2) *No more than 5% of the data points were identified as outliers.* Outliers include points flagged directly by the anemometer and points identified from the spike detection and removal filter detailed in Vickers and Mahrt (1997). All outliers were replaced by linear interpolation.

3) *No more than 25% change in mean wind speed and direction across the 5-min period.* The nonstationarity in mean conditions was determined from linear regression of the time series (Vickers and Mahrt 1997).

The data period was accepted if at least six of the eight sonic anemometers met all three criteria listed above. A majority of anemometers are required to ensure the flux profile fit detailed below produces a reliable result. For computing fluxes, turbulent fluctuations were estimated by subtracting the linear regression of each sonic anemometer time series.

The parameters h, u_*, and θ_* were then estimated from a nonlinear least squares fit of $\overline{u'w'}$ and $\overline{w'\theta'}$ to idealized flux profiles. The idealized profiles are assumed to be piecewise functions with $-\overline{u'w'} = u_*^2[1 - (z/h)]^{3/2}$ and $-\overline{w'\theta'} = u_*\theta_*[1 - (z/h)]$ for
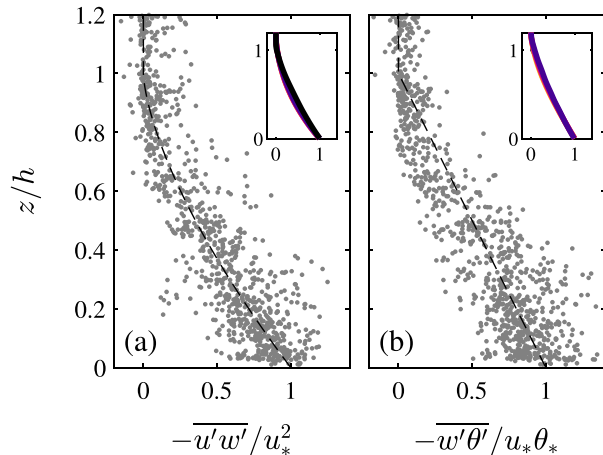
FIG. A1. Composite of dimensionless flux profiles for all accepted 5-min data periods from the CASES-99 field measurements: (a) momentum and (b) kinematic heat. The parameters h, u_*, and θ_* for each data period result from a least squares fit to the profiles $-\overline{u'w'}/u_*^2 = [1 - (z/h)]^{3/2}$ and $-\overline{w'\theta'}/u_*\theta_* = 1 - (z/h)$ (dashed lines), where zero flux is assumed above h. The inset panels show the corresponding LES profiles (solid lines).

$z \leq h$ (Nieuwstadt 1984), and $\overline{u'w'} = \overline{w'\theta'} = 0$ for $z > h$. The cost function for the fit is the residual between the computed fluxes and the piecewise profiles, where the residual considers both the momentum and kinematic heat fluxes simultaneously. Combining the two fluxes in the total residual ensures that the outputted parameters reflect both measured flux profiles.

Another consideration for the fitting procedure is the initial guesses for h, u_*, and θ_*. The output was found to be somewhat sensitive to arbitrary initial values, such that informed guesses are required. The initial values for u_* and θ_* are taken from the measured fluxes at the lowest height, and h is taken to be either the first height where the fluxes are less than 25% of the surface value or the top of the tower, whichever is lower.

Figure A1 shows the nondimensional flux profiles resulting from the fitting procedure, where the dashed lines represent the idealized piecewise functions. The choice of the fitted functions is supported by the LES flux profiles shown in the inset panels, where the profiles overlap closely with the piecewise functions such that the dashed lines are not visible. Revising the piecewise functions to assume a small nonzero flux above h (e.g., 5% of the surface value) does not change the conclusions of the analysis.

The fitted results were only accepted if $R^2 > 0.7$ based on the coefficient of determination. Importantly, the fitting procedure and R^2 threshold favor shallow boundary layers for which there is substantial flux decay across the height of the tower. For deeper boundary layers, it becomes harder to distinguish the more gradual flux decay from random error in the fluxes, leading to lower R^2 values that do not pass the threshold. This limitation can be accepted for the present analysis because the trends of interest occur in the strongly stable regime that is typically associated with a shallower SBL.
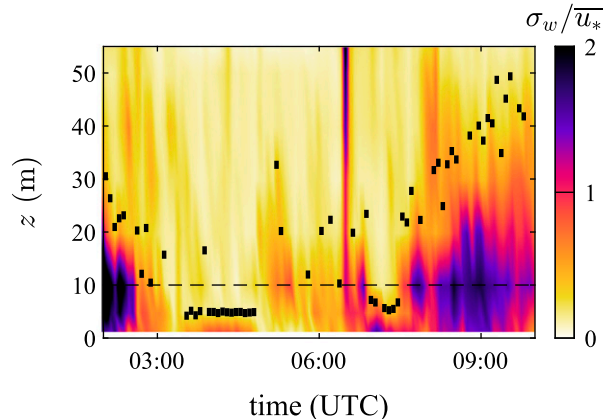

FIG. A2. Example space–time contour of the vertical root-mean-square velocity σ_w from the CASES-99 field measurements during a 10-h period on 18 Oct 1999, overlaid with the estimated boundary layer depth h for individual 5-min data periods. The values are shown relative to the average shear velocity $\overline{u_*}$ for the time period shown. The dashed line at $z = 10$ m is the minimum h considered in this study.

In addition to the R^2 criterion, minimum values were imposed for h, u_*, and θ_*. Fits with $h < 10$ m were excluded to avoid periods with a collapsed boundary layer and to ensure that at least three sonic anemometers were positioned within the SBL. Small flux values $u_*^2 < 0.0004$ m² s⁻² and $u_*\theta_* < 0.0004$ K m s⁻¹ were also excluded to avoid periods with very weak or intermittent turbulence. The sonic anemometers were a mixture of CSAT3 and ATI-K sonic anemometers, with the latter positioned at 10, 20, 40, and 55 m. The ATI-K sonic anemometers were found to have digitized values with a resolution of 0.01 for both velocity (m s⁻¹) and temperature (K). The CSAT3 sonic anemometers were rounded to the same resolution to compare computed fluxes from the coarsened signal with the original result. The relative error in the fluxes due to the digital resolution was less than 10% when the fluxes exceeded the minimum values above, which guided the selection of the threshold.

An example space–time contour of turbulent statistics for a 10-h period is shown in Fig. A2, where the statistics are computed in 5-min averaging intervals. The figure demonstrates how the fitted SBL depth h aligns well with the vertical position where the turbulent fluctuations become small relative to u_*. Figure A2 also illustrates multiple periods when turbulence collapses above the first measurement point such that the fitted depth is below the minimum threshold, i.e., the dashed line.

To estimate the gradient statistics, the mean profiles were fitted to the second-order polynomial $A + B\log(z) + C\log(z)^2$, and the derivatives were computed as $B/z + 2C\log(z)/z$ (Högström 1988). The mean velocity profiles used both the sonic and vane anemometers due to an observed agreement between the two instruments. The thermocouples were used for the mean temperature profiles to avoid drift issues associated with the sonic anemometers. The thermistor measurements were also used during occasional periods when

the thermocouples were unavailable. The least squares polynomial fits only considered points in the lowest 30% of the SBL relative to the fitted h. However, a minimum of four points was used in the case of a shallow SBL to avoid applying a three-parameter fit to three or fewer points. Mean profile fits with $R^2 < 0.9$ are excluded from the results presented here. From the fitted polynomial, the gradients were evaluated at the heights of the sonic anemometers to support the comparison of local-in-height scaling shown in Fig. 4.

Energy spectra were inspected for several of the accepted 5-min data subsets under strongly stable conditions. The spectra exhibited a canonical inertial subrange power law despite many of the periods having an estimated flux Richardson number above the critical value $\mathrm{Ri}_f \approx 0.2$ (Grachev et al. 2013). The discrepancy may be due to uncertainty in the estimated Ri_f values or the presence of nonlocal turbulent energy sources such as transport (Freire et al. 2019).

Of 7200 five-minute data subsets evaluated, 205 (2.9%) subsets met all the criteria above. Several tests were conducted to ensure the trends in Fig. 3 are not sensitive to the methodology. These tests include longer data periods, changes to the threshold values for maximum nonstationarity and profile fit R^2, finite difference estimates for gradients along $\log(z)$, and different methods for computing fluctuations. The use of longer data periods and stricter nonstationarity tests such as the reverse arrangement test (Dias et al. 2004), in combination with the flux profile fits, were found to eliminate too many data periods to discern any meaningful trend. Determination of a spectral gap and application of a high-pass filter to estimate fluxes (Vickers and Mahrt 2003) modestly reduces the scatter in the weakly stable regime, but the method employed here is preferred due to its simplicity. While the various tests changed the number of accepted data points and to a lesser extent the scatter, none of the tests yielded trends opposing the findings in section 3.

The depth h was alternatively estimated using lidar data and the height of detected LLJs (Banta et al. 2002). However, the LLJ was often far above the decay of fluxes and plateau of the mean profiles along the main met tower, consistent with previous findings (Banta et al. 2007). The observation suggests that the lowest LLJ that can be detected by the lidar is not always representative of the SBL depth, especially for strong stratification with a shallow SBL, such that the tower profile fits in Fig. A1 are preferred for the present study.

REFERENCES

Arya, S. P. S., 1977: Suggested revisions to certain boundary layer parameterization schemes used in atmospheric circulation models. *Mon. Wea. Rev.*, **105**, 215–227, https://doi.org/10.1175/1520-0493(1977)105<0215:SRTCBL>2.0.CO;2.

——, 1998: *Air Pollution Meteorology and Dispersion.* Oxford University Press, 320 pp.

Banta, R. M., R. K. Newsom, J. K. Lundquist, Y. L. Pichugina, R. L. Coulter, and L. Mahrt, 2002: Nocturnal low-level jet characteristics over Kansas during CASES-99. *Bound.-Layer*

Meteor., **105**, 221–252, https://doi.org/10.1023/A:1019992330866.

——, L. Mahrt, D. Vickers, J. Sun, B. B. Balsley, Y. L. Pichugina, and E. J. Williams, 2007: The very stable boundary layer on nights with weak low-level jets. *J. Atmos. Sci.*, **64**, 3068–3090, https://doi.org/10.1175/JAS4002.1.

Barenblatt, G. I., 2003: *Scaling.* Cambridge University Press, 171 pp., https://doi.org/10.1017/CBO9780511814921.

——, and V. Prostokishin, 1993: Scaling laws for fully developed turbulent shear flows. Part 2. Processing of experimental data. *J. Fluid Mech.*, **248**, 521–529, https://doi.org/10.1017/S0022112093000886.

Beare, R. J., and Coauthors, 2006: An intercomparison of large-eddy simulations of the stable boundary layer. *Bound.-Layer Meteor.*, **118**, 247–272, https://doi.org/10.1007/s10546-004-2820-6.

Beljaars, A. C. M., and A. A. M. Holtslag, 1991: Flux parameterization over land surfaces for atmospheric models. *J. Appl. Meteor.*, **30**, 327–341, https://doi.org/10.1175/1520-0450(1991)030<0327:FPOLSF>2.0.CO;2.

Brasseur, J. G., and T. Wei, 2010: Designing large-eddy simulation of the turbulent boundary layer to capture law-of-the-wall scaling. *Phys. Fluids*, **22**, 021303, https://doi.org/10.1063/1.3319073.

Buckingham, E., 1914: On physically similar systems; illustrations of the use of dimensional equations. *Phys. Rev.*, **4**, 345–376, https://doi.org/10.1103/PhysRev.4.345.

Businger, J. A., J. C. Wyngaard, Y. Izumi, and E. F. Bradley, 1971: Flux-profile relationships in the atmospheric surface layer. *J. Atmos. Sci.*, **28**, 181–189, https://doi.org/10.1175/1520-0469(1971)028<0181:FPRITA>2.0.CO;2.

Byun, D. W., 1991: Determination of similarity functions of the resistance laws for the planetary boundary layer using surface-layer similarity functions. *Bound.-Layer Meteor.*, **57**, 17–48, https://doi.org/10.1007/BF00119712.

Chamecki, M., N. L. Dias, and L. S. Freire, 2018: A TKE-based framework for studying disturbed atmospheric surface layer flows and application to vertical velocity variance over canopies. *Geophys. Res. Lett.*, **45**, 6734–6740, https://doi.org/10.1029/2018GL077853.

Chang, J. C., and S. R. Hanna, 2004: Air quality model performance evaluation. *Meteor. Atmos. Phys.*, **87**, 167–196, https://doi.org/10.1007/s00703-003-0070-7.

Cheng, Y., and W. Brutsaert, 2005: Flux-profile relationships for wind speed and temperature in the stable atmospheric boundary layer. *Bound.-Layer Meteor.*, **114**, 519–538, https://doi.org/10.1007/s10546-004-1425-4.

Delage, Y., 1974: A numerical study of the nocturnal atmospheric boundary layer. *Quart. J. Roy. Meteor. Soc.*, **100**, 351–364, https://doi.org/10.1002/qj.49710042507.

Deusebio, E., C. P. Caulfield, and J. R. Taylor, 2015: The intermittency boundary in stratified plane Couette flow. *J. Fluid Mech.*, **781**, 298–329, https://doi.org/10.1017/jfm.2015.497.

Dias, N. L., M. Chamecki, A. Kan, and C. M. P. Okawa, 2004: A study of spectra, structure and correlation functions and their implications for the stationarity of surface-layer turbulence. *Bound.-Layer Meteor.*, **110**, 165–189, https://doi.org/10.1023/A:1026067224894.

Donda, J. M. M., I. G. S. van Hooijdonk, A. F. Moene, H. J. J. Jonker, G. J. F. van Heijst, H. J. H. Clercx, and B. J. H. van de Wiel, 2014: Collapse of turbulence in stably stratified channel flow: A transient phenomenon. *Quart. J. Roy. Meteor. Soc.*, **141**, 2137–2147, https://doi.org/10.1002/qj.2511.

Du Vachat, R., and L. Musson-Genon, 1982: Rossby similarity and turbulent formulations. *Bound.-Layer Meteor.*, **23**, 47–68, https://doi.org/10.1007/BF00116111.

Dyer, A. J., 1974: A review of flux-profile relationships. *Bound.-Layer Meteor.*, **7**, 363–372, https://doi.org/10.1007/BF00240838.

Freire, L. S., M. Chamecki, E. Bou-Zeid, and N. L. Dias, 2019: Critical flux Richardson number for Kolmogorov turbulence enabled by TKE transport. *Quart. J. Roy. Meteor. Soc.*, **145**, 1551–1558, https://doi.org/10.1002/qj.3511.

Frenzen, P., and C. A. Vogel, 2001: Further studies of atmospheric turbulence in layers near the surface: Scaling the TKE budget above the roughness sublayer. *Bound.-Layer Meteor.*, **99**, 173–206, https://doi.org/10.1023/A:1018956931957.

Grachev, A. A., C. W. Fairall, P. O. G. Persson, E. L. Andreas, and P. S. Guest, 2005: Stable boundary-layer scaling regimes: The SHEBA data. *Bound.-Layer Meteor.*, **116**, 201–235, https://doi.org/10.1007/s10546-004-2729-0.

——, E. L. Andreas, C. W. Fairall, P. S. Guest, and P. O. G. Persson, 2007: SHEBA flux-profile relationships in the stable atmospheric boundary layer. *Bound.-Layer Meteor.*, **124**, 315–333, https://doi.org/10.1007/s10546-007-9177-6.

——, ——, ——, ——, and ——, 2013: The critical Richardson number and limits of applicability of local similarity theory in the stable boundary layer. *Bound.-Layer Meteor.*, **147**, 51–82, https://doi.org/10.1007/s10546-012-9771-0.

Gryning, S.-E., E. Batchvarova, B. Brümmer, H. Jørgensen, and S. Larsen, 2007: On the extension of the wind profile over homogeneous terrain beyond the surface boundary layer. *Bound.-Layer Meteor.*, **124**, 251–268, https://doi.org/10.1007/s10546-007-9166-9.

Ha, K.-J., Y.-K. Hyun, H.-M. Oh, K.-E. Kim, and L. Mahrt, 2007: Evaluation of boundary layer similarity theory for stable conditions in CASES-99. *Mon. Wea. Rev.*, **135**, 3474–3483, https://doi.org/10.1175/MWR3488.1.

Hartogensis, O. K., and H. A. R. de Bruin, 2005: Monin–Obukhov similarity functions of the structure parameter of temperature and turbulent kinetic energy dissipation rate in the stable boundary layer. *Bound.-Layer Meteor.*, **116**, 253–276, https://doi.org/10.1007/s10546-004-2817-1.

Heisel, M., T. Dasari, Y. Liu, J. Hong, F. Coletti, and M. Guala, 2018: The spatial structure of the logarithmic region in very-high-Reynolds-number rough wall turbulent boundary layers. *J. Fluid Mech.*, **857**, 704–747, https://doi.org/10.1017/jfm.2018.759.

——, C. M. de Silva, N. Hutchins, I. Marusic, and M. Guala, 2020: On the mixing length eddies and logarithmic mean velocity profile in wall turbulence. *J. Fluid Mech.*, **887**, R1, https://doi.org/10.1017/jfm.2020.23.

——, P. P. Sullivan, G. G. Katul, and M. Chamecki, 2023: Turbulence organization and mean profile shapes in the stably stratified boundary layer: Zones of uniform momentum and air temperature. *Bound.-Layer Meteor.*, **186**, 533–565, https://doi.org/10.1007/s10546-022-00771-0.

Hicks, B. B., 1981: An examination of turbulence statistics in the surface boundary layer. *Bound.-Layer Meteor.*, **21**, 389–402, https://doi.org/10.1007/BF00119281.

Högström, U., 1988: Non-dimensional wind and temperature profiles in the atmospheric surface layer: A re-evaluation. *Bound.-Layer Meteor.*, **42**, 55–78, https://doi.org/10.1007/BF00119875.

Holtslag, A. A. M., and F. T. M. Nieuwstadt, 1986: Scaling the atmospheric boundary layer. *Bound.-Layer Meteor.*, **36**, 201–209, https://doi.org/10.1007/BF00117468.

Howell, J. F., and J. Sun, 1999: Surface-layer fluxes in stable conditions. *Bound.-Layer Meteor.*, **90**, 495–520, https://doi.org/10.1023/A:1001788515355.

Jiménez, P. A., J. Dudhia, J. F. González-Rouco, J. Navarro, J. P. Montávez, and E. García-Bustamante, 2012: A revised scheme for the WRF surface layer formulation. *Mon. Wea. Rev.*, **140**, 898–918, https://doi.org/10.1175/MWR-D-11-00056.1.

Johansson, C., A.-S. Smedman, U. Högström, J. G. Brasseur, and S. Khanna, 2001: Critical test of the validity of Monin–Obukhov similarity during convective conditions. *J. Atmos. Sci.*, **58**, 1549–1566, https://doi.org/10.1175/1520-0469(2001)058<1549:CTOTVO>2.0.CO;2.

Kenney, B. C., 1982: Beware of spurious self-correlations! *Water Resour. Res.*, **18**, 1041–1048, https://doi.org/10.1029/WR018i004p01041.

Khanna, S., and J. G. Brasseur, 1997: Analysis of Monin–Obukhov similarity from large-eddy simulation. *J. Fluid Mech.*, **345**, 251–286, https://doi.org/10.1017/S0022112097006277.

Kitaigorodskii, S. A., 1960: On the computation of the thickness of the wind-mixing layer in the ocean. *Izv. Akad. Nauk SSSR, Ser. Geofiz.*, **3**, 425–431.

——, and S. M. Joffre, 1988: In search of a simple scaling for the height of the stratified atmospheric boundary layer. *Tellus*, **40A**, 419–433, https://doi.org/10.3402/tellusa.v40i5.11812.

Klipp, C. L., and L. Mahrt, 2004: Flux–gradient relationship, self-correlation and intermittency in the stable boundary layer. *Quart. J. Roy. Meteor. Soc.*, **130**, 2087–2103, https://doi.org/10.1256/qj.03.161.

Kosović, B., and J. A. Curry, 2000: A large eddy simulation study of a quasi-steady, stably stratified atmospheric boundary layer. *J. Atmos. Sci.*, **57**, 1052–1068, https://doi.org/10.1175/1520-0469(2000)057<1052:ALESSO>2.0.CO;2.

Kouznetsov, R. D., and S. S. Zilitinkevich, 2010: On the velocity gradient in stably stratified sheared flows. Part 2: Observations and models. *Bound.-Layer Meteor.*, **135**, 513–517, https://doi.org/10.1007/s10546-010-9487-y.

LeHau, H. H., 1959: Wind profile, surface stress and geostrophic drag coefficients in the atmospheric surface layer. *Adv. Geophys.*, **6**, 241–257, https://doi.org/10.1016/S0065-2687(08)60111-9.

Li, D., S. Salesky, and T. Banerjee, 2016: Connections between the Ozmidov scale and mean velocity profile in stably stratified atmospheric surface layers. *J. Fluid Mech.*, **797**, R3, https://doi.org/10.1017/jfm.2016.311.

Mahrt, L., 1999: Stratified atmospheric boundary layers. *Bound.-Layer Meteor.*, **90**, 375–396, https://doi.org/10.1023/A:1001765727956.

——, 2007: The influence of nonstationarity on the turbulent flux-gradient relationship for stable stratification. *Bound.-Layer Meteor.*, **125**, 245–264, https://doi.org/10.1007/s10546-007-9154-0.

——, and O. Acevedo, 2023: Types of vertical structure of the nocturnal boundary layer. *Bound.-Layer Meteor.*, **187**, 141–161, https://doi.org/10.1007/s10546-022-00716-7.

Manwell, J. F., J. G. McGowan, and A. L. Rogers, 2009: *Wind Energy Explained: Theory, Design, and Application.* 2nd ed. John Wiley and Sons, 704 pp.

Marusic, I., J. P. Monty, M. Hultmark, and A. J. Smits, 2013: On the logarithmic region in wall turbulence. *J. Fluid Mech.*, **716**, R3, https://doi.org/10.1017/jfm.2012.511.

Mason, P. J., and D. J. Thomson, 1992: Stochastic backscatter in large-eddy simulations of boundary layers. *J. Fluid Mech.*, **242**, 51–78, https://doi.org/10.1017/S0022112092002271.

McVehil, G. E., 1964: Wind and temperature profiles near the ground in stable stratification. *Quart. J. Roy. Meteor. Soc.*, **90**, 136–146, https://doi.org/10.1002/qj.49709038403.

Melgarejo, J. W., and J. W. Deardorff, 1974: Stability functions for the boundary-layer resistance laws based upon observed boundary-layer heights. *J. Atmos. Sci.*, **31**, 1324–1333, https://doi.org/10.1175/1520-0469(1974)031<1324:SFFTBL>2.0.CO;2.

Millikan, C. M., 1938: A critical discussion of turbulent flows in channels and circular tubes. *Proc. Fifth Int. Congress for Applied Mechanics*, Cambridge, MA, ICAM, 386–392.

Mironov, D., and E. Fedorovich, 2010: On the limiting effect of the Earth's rotation on the depth of a stably stratified boundary layer. *Quart. J. Roy. Meteor. Soc.*, **136**, 1473–1480, https://doi.org/10.1002/qj.631.

Moeng, C.-H., and J. C. Wyngaard, 1988: Spectral analysis of large-eddy simulations of the convective boundary layer. *J. Atmos. Sci.*, **45**, 3573–3587, https://doi.org/10.1175/1520-0469(1988)045<3573:SAOLES>2.0.CO;2.

Monahan, A. H., T. Rees, Y. He, and N. McFarlane, 2015: Multiple regimes of wind, stratification, and turbulence in the stable boundary layer. *J. Atmos. Sci.*, **72**, 3178–3198, https://doi.org/10.1175/JAS-D-14-0311.1.

Monin, A. S., and A. M. Obukhov, 1954: Basic laws of turbulent mixing in the atmosphere near the ground. *Tr. Geofiz. Inst., Akad. Nauk SSSR*, **24**, 163–187.

Nieuwstadt, F. T. M., 1984: The turbulent structure of the stable, nocturnal boundary layer. *J. Atmos. Sci.*, **41**, 2202–2216, https://doi.org/10.1175/1520-0469(1984)041<2202:TTSOTS>2.0.CO;2.

——, and H. Tennekes, 1981: A rate equation for the nocturnal boundary-layer height. *J. Atmos. Sci.*, **38**, 1418–1428, https://doi.org/10.1175/1520-0469(1981)038<1418:AREFTN>2.0.CO;2.

Obukhov, A. M., 1971: Turbulence in an atmosphere with a non-uniform temperature. *Bound.-Layer Meteor.*, **2**, 7–29, https://doi.org/10.1007/BF00718085.

Oke, T. R., 1970: Turbulent transport near the ground in stable conditions. *J. Appl. Meteor.*, **9**, 778–786, https://doi.org/10.1175/1520-0450(1970)009<0778:TTNTGI>2.0.CO;2.

Optis, M., A. Monahan, and F. C. Bosveld, 2014: Moving beyond Monin–Obukhov similarity theory in modelling wind-speed profiles in the lower atmospheric boundary layer under stable stratification. *Bound.-Layer Meteor.*, **153**, 497–514, https://doi.org/10.1007/s10546-014-9953-z.

Poulos, G. S., and Coauthors, 2002: CASES-99: A comprehensive investigation of the stable nocturnal boundary layer. *Bull. Amer. Meteor. Soc.*, **83**, 555–582, https://doi.org/10.1175/1520-0477(2002)083<0555:CACIOT>2.3.CO;2.

Prandtl, L., 1932: Zur turbulenten strömung in röhren und längs platten. *Ergebnisse der aerodynamischen Versuchsanstalt zu Göttingen*, Vol. 4, Oldenbourg Wissenschaftsverlag, 18–29.

Rossby, C., and R. B. Montgomery, 1935: The layer of frictional influence in wind and ocean currents. *Pap. Phys. Oceanogr. Meteor.*, **3**, 101, https://doi.org/10.1575/1912/1157.

Saddoughi, S. G., and S. V. Veeravalli, 1994: Local isotropy in turbulent boundary layers at high Reynolds number. *J. Fluid Mech.*, **268**, 333–372, https://doi.org/10.1017/S0022112094001370.

Salesky, S. T., and M. Chamecki, 2012: Random errors in turbulence measurements in the atmospheric surface layer: Implications for Monin–Obukhov similarity theory. *J. Atmos. Sci.*, **69**, 3700–3714, https://doi.org/10.1175/JAS-D-12-096.1.

——, and W. Anderson, 2020: Coherent structures modulate atmospheric surface layer flux-gradient relationships. *Phys. Rev. Lett.*, **125**, 124501, https://doi.org/10.1103/PhysRevLett.125.124501.

Simiu, E., and D. H. Yeo, 2019: *Wind Effects on Structures: Modern Structural Design for Wind*. 4th ed. Wiley-Blackwell, 520 pp.

Sorbjan, Z., 1986: On similarity in the atmospheric boundary layer. *Bound.-Layer Meteor.*, **34**, 377–397, https://doi.org/10.1007/BF00120989.

Sullivan, P. P., J. C. Weil, E. G. Patton, H. J. J. Jonker, and D. V. Mironov, 2016: Turbulent winds and temperature fronts in large-eddy simulations of the stable atmospheric boundary layer. *J. Atmos. Sci.*, **73**, 1815–1840, https://doi.org/10.1175/JAS-D-15-0339.1.

Sun, J., and Coauthors, 2002: Intermittent turbulence associated with a density current passage in the stable boundary layer. *Bound.-Layer Meteor.*, **105**, 199–219, https://doi.org/10.1023/A:1019969131774.

Townsend, A. A., 1976: *The Structure of Turbulent Shear Flow*. 2nd ed. Cambridge University Press, 429 pp.

van de Wiel, B. J. H., A. F. Moene, G. J. Steeneveld, O. K. Hartogensis, and A. A. M. Holtslag, 2007: Predicting the collapse of turbulence in stably stratified boundary layers. *Flow, Turbul. Combust.*, **79**, 251–274, https://doi.org/10.1007/s10494-007-9094-2.

Vickers, D., and L. Mahrt, 1997: Quality control and flux sampling problems for tower and aircraft data. *J. Atmos. Oceanic Technol.*, **14**, 512–526, https://doi.org/10.1175/1520-0426(1997)014<0512:QCAFSP>2.0.CO;2.

——, and ——, 2003: The cospectral gap and turbulent flux calculations. *J. Atmos. Oceanic Technol.*, **20**, 660–672, https://doi.org/10.1175/1520-0426(2003)20<660:TCGATF>2.0.CO;2.

von Kármán, T., 1930: Mechanische Ähnlichkeit und Turbulenz. *Nachr. Ges. Wiss. Göettingen Math. Phys. Kl.*, **68**, 58–76.

Webb, E. K., 1970: Profile relationships: The log-linear range, and extension to strong stability. *Quart. J. Roy. Meteor. Soc.*, **96**, 67–90, https://doi.org/10.1002/qj.49709640708.

Williams, A. G., S. Chambers, and A. Griffiths, 2013: Bulk mixing and decoupling of the nocturnal stable boundary layer characterized using a ubiquitous natural tracer. *Bound.-Layer Meteor.*, **149**, 381–402, https://doi.org/10.1007/s10546-013-9849-3.

Wyngaard, J. C., 1992: Atmospheric turbulence. *Annu. Rev. Fluid Mech.*, **24**, 205–234, https://doi.org/10.1146/annurev.fl.24.010192.001225.

——, and O. R. Coté, 1971: The budgets of turbulent kinetic energy and temperature variance in the atmospheric surface layer. *J. Atmos. Sci.*, **28**, 190–201, https://doi.org/10.1175/1520-0469(1971)028<0190:TBOTKE>2.0.CO;2.

——, and ——, 1972: Cospectral similarity in the atmospheric surface layer. *Quart. J. Roy. Meteor. Soc.*, **98**, 590–603, https://doi.org/10.1002/qj.49709841708.

Yaglom, A. M., 1977: Comments on wind and temperature flux-profile relationships. *Bound.-Layer Meteor.*, **11**, 89–102, https://doi.org/10.1007/BF00221826.

Yamada, T., 1976: On the similarity functions A, B and C of the planetary boundary layer. *J. Atmos. Sci.*, **33**, 781–793, https://doi.org/10.1175/1520-0469(1976)033<0781:OTSFAO>2.0.CO;2.

Zilitinkevich, S. S., 1989: Velocity profiles, the resistance law and the dissipation rate of mean flow kinetic energy in a neutrally and stably stratified boundary layer. *Bound.-Layer Meteor.*, **46**, 367–387, https://doi.org/10.1007/BF00172242.

——, and D. V. Chalikov, 1968: Determining the universal wind-velocity and temperature profiles in the atmospheric boundary layer. *Izv. Atmos. Ocean. Phys.*, **4**, 194–302.

——, and D. V. Mironov, 1996: A multi-limit formulation for the equilibrium depth of a stably stratified boundary layer. *Bound.-Layer Meteor.*, **81**, 325–351, https://doi.org/10.1007/BF02430334.

——, and P. Calanca, 2000: An extended similarity theory for the stably stratified atmospheric surface layer. *Quart. J. Roy. Meteor. Soc.*, **126**, 1913–1923, https://doi.org/10.1256/smsqj.56617.

——, and I. N. Esau, 2005: Resistance and heat-transfer laws for stable and neutral planetary boundary layers: Old theory advanced and re-evaluated. *Quart. J. Roy. Meteor. Soc.*, **131**, 1863–1892, https://doi.org/10.1256/qj.04.143.